

High throughput discovery of functional protein modifications by Hotspot Thermal Profiling

Jun X. Huang^{1,2}, Gihoon Lee^{1,2}, Kate E. Cavanaugh^{3,4,5}, Jae W. Chang^{1,2}, Margaret L. Gardel^{3,4,5} and Raymond E. Moellering^{1,2*}

Mass spectrometry enables global analysis of posttranslationally modified proteoforms from biological samples, yet we still lack methods to systematically predict, or even prioritize, which modification sites may perturb protein function. Here we describe a proteomic method, Hotspot Thermal Profiling, to detect the effects of site-specific protein phosphorylation on the thermal stability of thousands of native proteins in live cells. This massively parallel biophysical assay unveiled shifts in overall protein stability in response to site-specific phosphorylation sites, as well as trends related to protein function and structure. This method can detect intrinsic changes to protein structure as well as extrinsic changes to protein–protein and protein–metabolite interactions resulting from phosphorylation. Finally, we show that functional ‘hotspot’ protein modification sites can be discovered and prioritized for study in a high-throughput and unbiased fashion. This approach is applicable to diverse organisms, cell types and posttranslational modifications.

The posttranslational modification (PTM) of protein backbone and side chains affects the function of target proteins by perturbing the three-dimensional structure of the protein itself, as well as by altering intermolecular interactions with other biomolecules. PTMs regulate protein–protein interactions¹, subcellular compartmentalization², substrate and cofactor interactions, protein turnover³ and other functions, to collectively impact normal⁴ and dysregulated^{5–7} signal transduction in cells.

The quantitative interrogation of endogenous PTMs has been greatly accelerated by methods such as liquid chromatography–mass spectrometry (LC–MS)⁸. Subsequent integration of front-end, PTM-specific enrichment protocols with data-dependent and de novo PTM discovery algorithms has resulted in the discovery of tens of thousands of unique PTM sites on proteins from diverse organisms^{9–11}, as well as quantification of PTM dynamics in diverse biological contexts and responses to stimuli^{12–14}. Central questions around how minute changes to chemical structure alter the biophysical properties of a much larger protein, and how these changes lead to signaling and phenotypic consequences, remain only partially explored. This dearth of mechanistic information on PTMs exists because we lack general methods with which to predict, or even prioritize, which modification sites are likely to be functional in the proteome, and, therefore, the one-by-one study of PTMs is intrinsically inefficient and low throughput.

Here we sought to develop a proteomic method that enables direct interrogation of protein stability in response to endogenous PTMs, for thousands of proteins in parallel. This method, Hotspot Thermal Profiling (HTP), couples PTM-specific enrichments and isotopic labeling with global profiling by liquid chromatography–tandem mass spectrometry (LC–MS/MS) to measure the thermal stability of endogenous modified proteoforms, which we refer to as ‘modiforms’, in live cells (Fig. 1). We apply this approach to a ubiquitous yet diminutive PTM (namely, phosphorylation) and demonstrate that HTP can detect both inter- and intramolecular interactions mediated by site-specific PTMs on a wide range of

proteins. Moreover, we demonstrate that perturbation of protein stability can be used as a means to discover functionally important and previously uncharacterized ‘hotspot’ modification sites. The resulting dataset represents a rich and generalizable resource to prioritize existing datasets of phosphorylation sites in diverse biological contexts.

Results

HTP detects changes in protein stability in response to site-specific modification. The HTP workflow begins with pulsed exposure of live cell aliquots to temperatures ranging from 37 to 67 °C for 3 min, cooling to room temperature, rapid cell lysis and centrifugation to remove unfolded proteins, in line with reports mapping ligand–protein^{15–18} and protein–protein¹⁹ interactions by thermal proteome profiling (Fig. 1a). The soluble proteome of each aliquot is then proteolyzed and 5% of each peptide aliquot is labeled with specific tandem mass tag (TMT) isotope channels and reserved for quantification of the ‘unmodified, bulk’ protein pool (Fig. 1a). The remaining 95% of each aliquot is used for phosphopeptide enrichment by TiO₂ resin, followed by TMT isotope labeling (Fig. 1b). All aliquots of the unenriched and phosphorylated TMT tryptic peptides are subsequently combined and used for LC–MS/MS detection and quantitation of relative peptide levels across the temperature range.

Peptide-level measurements are analyzed en masse with identification, quantification and automated curve-fitting algorithms to generate peptide-specific melting points (T_m) for tens of thousands of unique peptides per sample (Fig. 1a). Because quantitative proteomic measurements are performed on individual peptides, measurements made on a unique modified peptide (for example, a phosphorylated peptide) serve as a ‘bar code’ to report on any protein that contains a modification at that site to the thermal challenge in live cells. Therefore, this method does not report on single ‘proteoforms’ as recently defined²⁰, but instead reports on an inclusive set of the protein pool that is unambiguously phosphorylated at the

¹Department of Chemistry, The University of Chicago, Chicago, IL, USA. ²Institute for Genomics and Systems Biology, The University of Chicago, Chicago, IL, USA. ³Department of Physics, The University of Chicago, Chicago, IL, USA. ⁴Institute for Biophysical Dynamics, The University of Chicago, Chicago, IL, USA. ⁵James Franck Institute, The University of Chicago, Chicago, IL, USA. *e-mail: rmoellering@uchicago.edu

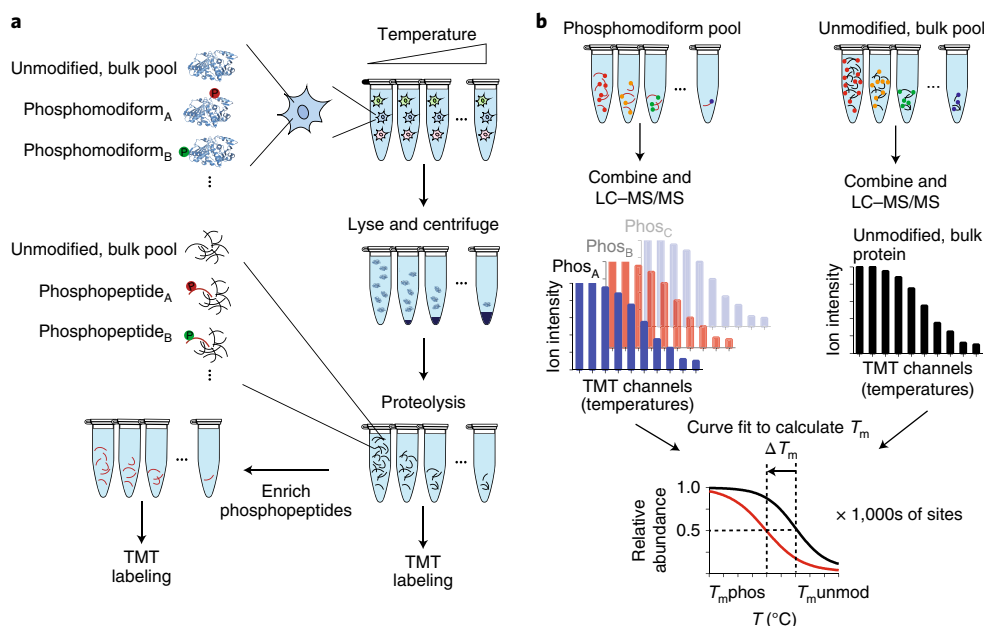


Fig. 1 | HTP workflow. **a**, Aliquots of live cells are exposed to short, varied temperature challenge, lysed and soluble/insoluble proteins are separated by ultracentrifugation. Downstream trypsinization and separation of aliquots for bulk proteome (5%) and phosphopeptide enrichment (95%) differentiates bulk, unmodified and phosphomodiform interrogation. **b**, Bulk and enriched peptide aliquots are labeled with unique tandem mass tag channels, pooled and analyzed by LC-MS/MS. The output of each MS run is searched using an integrated platform for peptide identification and quantification, T_m curve fitting and integration for bulk, unmodified protein (Unmod) or modification site level (Phos) T_m determination. Unique phosphomodiforms and their corresponding phosphopeptides are abbreviated as Phos_A, Phos_B...Phos_X.

detected site, which we define as the ‘phosphomodiform’. This is a key differentiation from measuring the effect of a modification on the bulk protein pool, such that HTP can detect altered thermal stability even if a modiform is only a minor member of all the modified proteoforms present in the cell (Fig. 1b).

We applied the HTP workflow to detect the T_m values of phosphomodiforms and the bulk, unmodified protein pool in HEK293T cells. We detected >250,000 TMT-labeled peptides from thousands of proteins across a handful of LC-MS/MS runs (Supplementary Fig. 1), and statistical filtering through identification, quantification and curve fitting were combined to generate 4,293 ‘unmodified, bulk’ protein T_m values (Fig. 2a,b). Here we define the unmodified, bulk as all unmodified peptides that map to a given protein of interest, such that this T_m reflects the ‘reference’ population of protein present in cells. Protein and peptide T_m measurements were highly stable across replicates, validating the reproducibility of cellular- and proteome-level manipulations in the HTP workflow, and indicating that even small shifts in thermal stability (for example, ~1.5 °C) can be reliably detected with statistical significance (Supplementary Fig. 2a–f).

To measure phosphomodiform-specific T_m values, we integrated metal-dependent phosphopeptide enrichment with subsequent TMT barcoding (Fig. 1). Global phosphorylation was not grossly affected by the short exposure to varied temperature (Supplementary Fig. 3).

Duplicate technical replicates from five biological replicates ($n = 10$ LC-MS/MS runs), as well as grouping phosphopeptides that map to a common site (Supplementary Fig. 4), resulted in identification of 10,800 phosphomodiforms. Automated T_m curve-fitting cutoffs ($R^2 > 0.8$) resulted in a dataset of 9,695 distinct phosphomodiforms. Finally, filtering of only high-confidence T_m values detected in both phospho- and unmodified, bulk proteomes, as well as stringent modification site localization validation²¹, yielded 2,883 high-quality ΔT_m values that directly compare a specific phosphomodiform to its unmodified, bulk protein (Fig. 2a,b and Supplementary Table 1).

The unmodified and phosphorylated proteomes were globally indistinguishable, with mean T_m values of 51.2 and 51.0 °C, respectively (Fig. 2b). By contrast, comparison of a given protein to its specific phosphomodiforms yielded a diverse ΔT_m profile that was Gaussian in nature, and highlighted the fact that the most phosphorylated modiforms did not exhibit altered thermal stability relative to their parent proteins (Fig. 2c and Supplementary Table 2). There were a sizable number of phosphosites, however, associated with markedly different thermal stability compared with their unmodified, bulk protein pool in live cells (Fig. 2c). A detailed analysis of specific temperature–response curves verified these trends, with many parent protein–phosphomodiform pairs producing sigmoidal curves that overlay almost exactly (Fig. 2d). In contrast, numerous phosphomodiforms exhibited significantly different temperature–response curves compared with their unmodified, bulk protein counterpart, including pY15 on cyclin-dependent kinase CDK1 and pT926 on kinesin-like protein KIF11 (Fig. 2e,f). Both of these sites have critical roles in regulating the function of their target protein: pY15 has been shown to inactivate CDK1 through structural reorganization and autoinhibition^{22,23}, while pT926 controls intermolecular association of KIF11 with the spindle apparatus during mitosis²⁴.

The phosphosite-specific resolution of HTP contrasts with previous reports that have detected shifts in bulk protein T_m values in response to phosphorylation as indirect but related targets of drug action^{18,19,25}. Instead, the direct interrogation of phosphomodiforms with amino-acid resolution validates the ability to distinguish functional effects at different modification sites, as well as minor phosphomodiforms that might otherwise be masked by more abundant proteoforms. For example, the pS58 phosphomodiform of the enzyme TPI1 is associated with significant destabilization, while pT210 has no effect on its stability (Fig. 2g). These data confirmed that modification-dependent changes in protein stability can be detected by thermal profiling of the modified proteome. Most importantly, we hypothesized that ‘hotspot’ modification sites

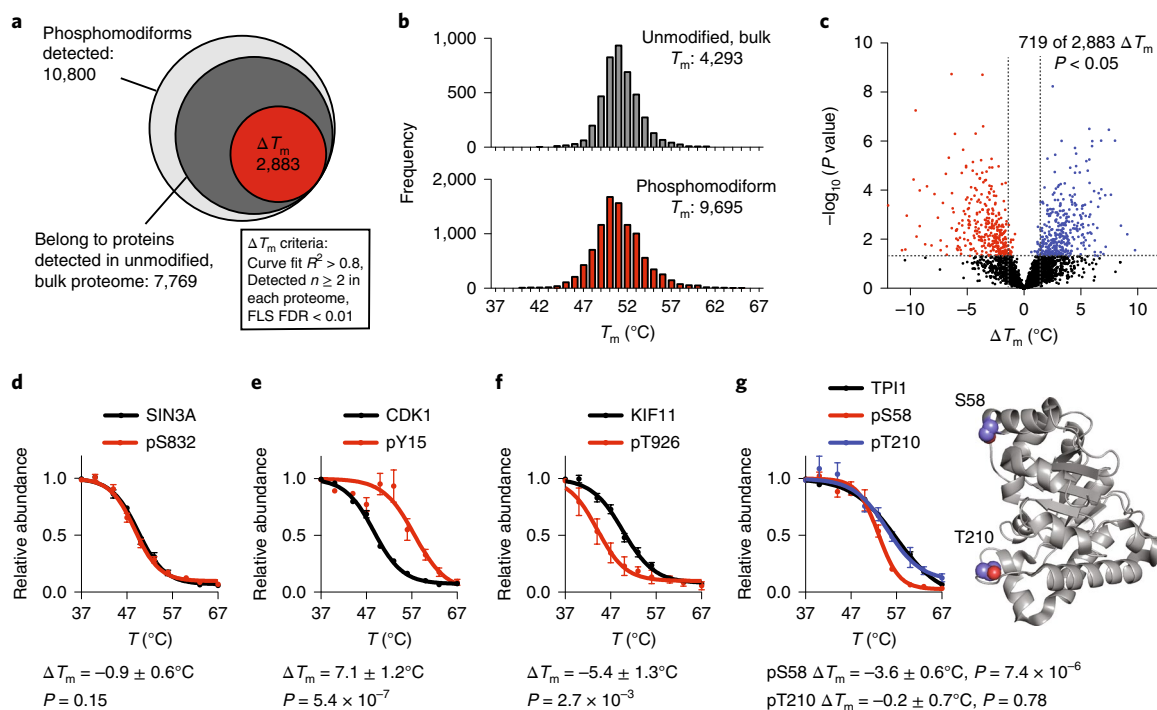


Fig. 2 | HTP identifies thousands of unmodified, bulk and phosphomodiform T_m values in HEK293T cells. **a**, The total number of unique phosphomodiforms detected in our dataset and the criteria for identifying high-quality ΔT_m values. FLS FDR, localization site false discovery rate. **b**, Global distribution of unmodified, bulk protein level and phosphomodiform T_m values. **c**, Volcano plot of high-confidence ΔT_m values. Phosphomodiforms with significant shifts ($P < 0.05$, two-sided t -test for within-protein comparisons) are shown in red (negative shift) and blue (positive shift). **d–g**, Representative T_m curves from phosphomodiforms that do not affect (**d**), increase (**e**) and decrease (**f**) thermal stability. Distinct phosphomodiforms of the same protein that exhibit unique ΔT_m values, as exemplified in TPI1 (**g**). Detected phosphorylation sites in TPI1 are shown as spheres; PDB 1WYI. T_m curves and error bars in **d–g** correspond to mean and s.e.m. from $n = 12, 10, 6, 4, 12, 2, 12, 10$ and 4 replicate measurements (in order of T_m curve appearance, top to bottom, left to right). All data were generated from $n = 12$ (bulk, unmodified) and $n = 10$ (phospho) total MS technical replicates from $n = 6$ (bulk, unmodified) and 5 (phospho) independent biological replicates. ΔT_m P values computed with two-sided t -test.

identified in this screen (namely, those significantly shifted relative to the unmodified, bulk and even other phosphomodiforms of the same protein) may represent sites with disproportionate effects on protein structure and function under specific cellular conditions.

Perturbation of protein stability by phosphorylation is site-specific, not systematic. We next asked whether there were any systematic correlations between the types and contexts of protein phosphorylation sites and their effect on protein stability. Comparison of the ΔT_m values for phosphorylation on different residues (serine, threonine and tyrosine) across all detected phosphomodiforms did not reveal any general bias for stabilization or destabilization (Fig. 3a). Classes of modifforms harboring multiple phosphorylation sites within the same peptide, and therefore in high proximity on the protein, were also not significantly associated with increased or decreased stability. Global ΔT_m values among phosphorylation sites in established kinase motifs also did not reveal significant correlations, indicating that the combination of phosphoamino acid and directly adjacent sequence context does not, at least on a global average in this dataset, impart a systematic stabilizing or destabilizing effect (Fig. 3a,b). As expected, phosphosites detected in our dataset showed enrichment in predicted loop or coil secondary structural elements (Fig. 3c)^{26–28}. Relative to the majority of sites in coil/loop regions, phosphosites within predicted helical or β -sheet secondary structures demonstrated decreased stability, on average (Fig. 3d). Furthermore, a significant stabilizing trend was observed for phosphosites located in exposed protein regions, relative to those located in buried regions, as determined by computational predictions of solvent accessibility and local

structure organization (Fig. 3e,f). These global trends imply that the effect of protein phosphorylation (as far as can be deduced with this method) is governed by local context within proteins, as opposed to a systemic, biophysical ‘code’ imparted by the phosphoamino acid or linear motif.

HTP detects phosphorylation-mediated protein–protein interactions. We next asked whether significantly perturbed ‘hotspot’ ΔT_m values were correlated with altered intra- or intermolecular interactions in cells, or with both. Global correlation of phosphorylation site ΔT_m and the number of functional annotations present in the PhosphoSite online database highlighted that most sites (92.5%) detected in this dataset had no annotation, as is true for the vast majority of known posttranslational modification sites in the human proteome²⁹. Well-characterized, functional sites in proteins, such as CDK1, STAT3 and STAT1, stood out on this annotation plot (Fig. 4a). Additionally, a cluster of highly perturbed and well-annotated sites in the eukaryotic translation initiation factor 4E binding protein 1 (4EBP1) were conspicuous.

The unmodified, bulk 4EBP1 pool exhibited a T_m of $53.8 \pm 0.8^\circ\text{C}$ by HTP (Fig. 4b), whereas the phosphomodiforms containing phosphorylation sites in the amino (N)-terminal region were significantly less stable (Fig. 4b). These sites were clustered in a region known to be responsible for direct binding to eukaryotic translation initiation factor 4E (EIF4E), which prevents ribosome binding and translation^{30,31}. A phosphorylation cascade that requires T37, T46 and intervening phosphorylation sites as initiating modifications lead to phosphorylation of Y54, which blocks 4EBP1 binding to EIF4E³². The thermal shifts resulting from phosphorylation around

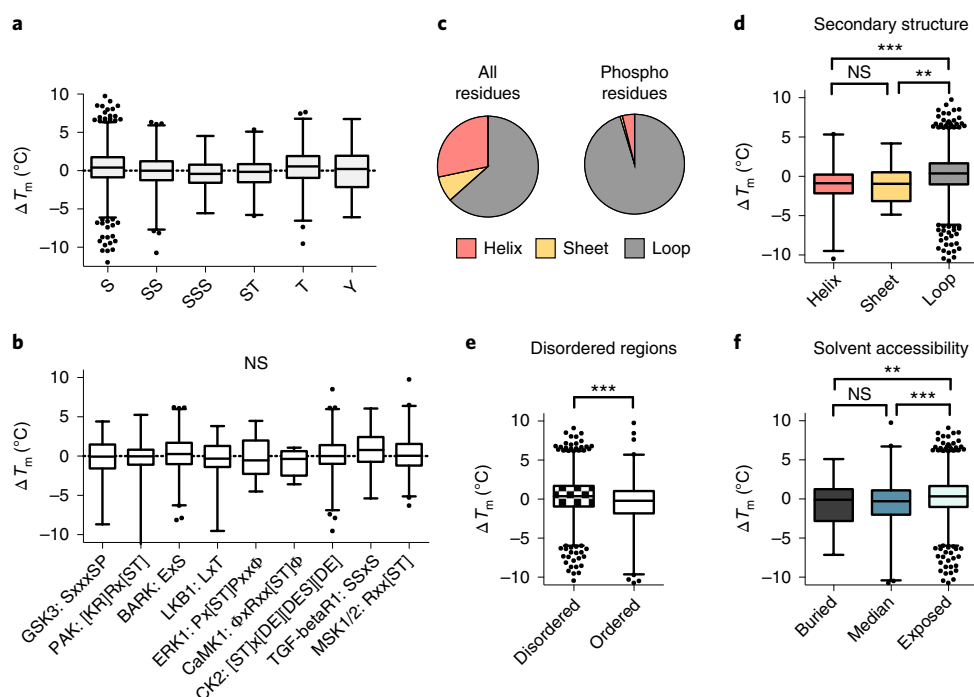


Fig. 3 | Global relationships between local phosphosite environment and altered phosphomodform stability. **a**, Distribution of ΔT_m values for tryptic peptides containing indicated phosphoamino acids or coincidental combinations thereof ($P < 0.0001$, one-way analysis of variance (ANOVA)). **b**, Correlation between detected kinase substrate motifs and ΔT_m values for identified sites ($P = 0.3011$, one-way ANOVA). **c**, Distribution of all amino acids in the human proteome (left) and detected phosphosites (right) in predicted secondary structural elements. **d–f**, Comparisons of ΔT_m values and predicted secondary structure elements (**d**; $***P \leq 0.0001$, $**P \leq 0.001$ two-sided t -test), ordered structural elements surrounding the phosphosite of interest (**e**; $***P \leq 0.0001$, two-sided t -test) and solvent accessibility (**f**; $***P \leq 0.0001$, $**P \leq 0.001$ two-sided t -test). Box plots (median, 1–99%) are shown in **a, b, d–f**, with outliers shown as data points. All data were generated from $n = 12$ (bulk, unmodified) and $n = 10$ (phospho) total MS technical replicates from $n = 6$ (bulk, unmodified) and $n = 5$ (phospho) independent biological replicates.

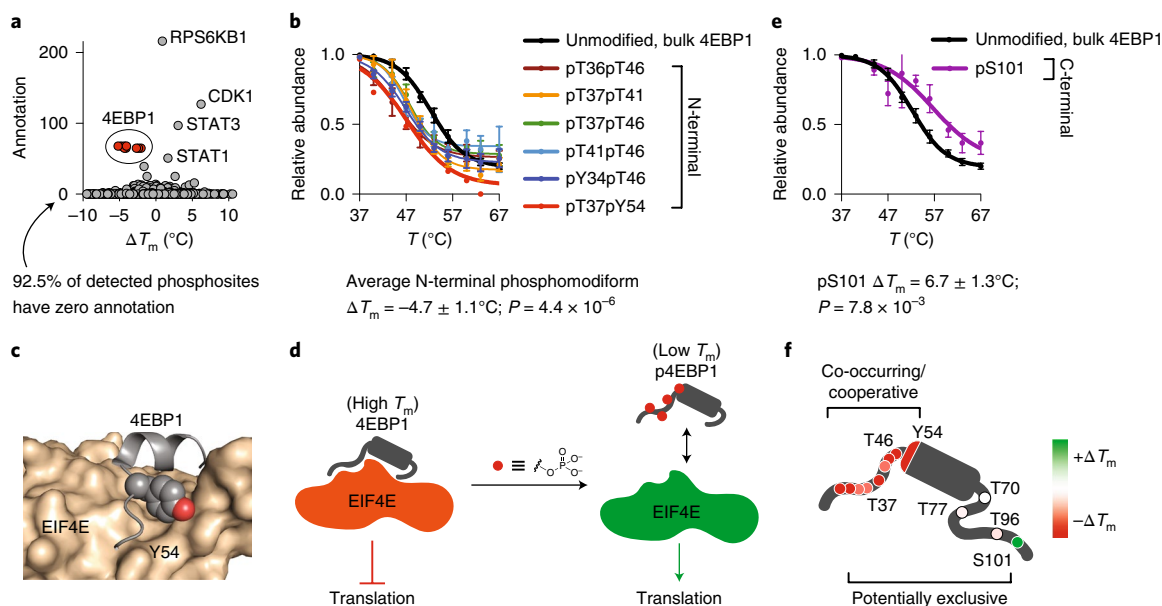


Fig. 4 | HTP detects the known 4EBP1-EIF4E protein-protein interaction mediated by phosphorylation. **a**, Plot of phosphosite ΔT_m and number of annotations in the PhosphoSite online database. A cluster of 4EBP1 phosphosites are highlighted in red. **b**, Representative subset of HTP curves for the unmodified, bulk and N-terminal phosphomodforms of 4EBP1. **c**, X-ray structure of the N-terminal helix-turn motif of 4EBP1 (gray) bound to EIF4E (tan); Y54 in 4EBP1 is shown as spheres. **d**, Proposed model correlating observed thermal stability shifts to 4EBP1-EIF4E complexes. **e**, HTP curve for C-terminal pS101 phosphomodform. **f**, Schematic showing the location and relative ΔT_m values for all detected phosphomodforms of 4EBP1, with annotation of potentially co-occurring and exclusive modification patterns based on thermal response. Data points shown in **b, e** represent the mean and s.e.m. from $n = 12, 6, 9, 6, 3, 6, 1, 12$ and 2 (in order of T_m curve appearance) replicate measurements detected in $n = 6$ (bulk, unmodified) and $n = 5$ (phospho) independent biological replicates. ΔT_m P values were calculated with two-sided t -tests.

this site are consistent with steric and electronic perturbation of the peptide surrounding Y54 binding the hydrophobic ledge in EIF4E (Fig. 4c), which further suggests that the shift in thermal stability observed for phosphorylated 4EBP1 modifforms may be measuring the bound and unbound forms of this protein on a macromolecular complex, respectively. In this model, 4EBP1 proteins lacking N-terminal phosphorylation demonstrate higher thermal stability due to involvement in the protein–protein interaction with EIF4E, and likely other members of a macromolecular complex. This is contrasted by significantly reduced thermal stability of N-terminal phosphorylated modifforms that are not engaged in this interaction, and are either free in solution or engaged in an alternative set of interactions (Fig. 4d).

While the data provided by HTP global analysis cannot distinguish these scenarios per se, this method is able to detect these previously annotated functional ‘hotspot’ sites in a global, unbiased manner, and indicate that HTP can detect the consequences of altered intermolecular interactions, which would be impossible to identify in purely *in vitro* systems. Extending this analysis of 4EBP1, HTP profiling also detected distinct phosphomodifforms, including 4EBP1 phosphorylated at S101, which is associated with increased stability (Fig. 4e). The ability to detect unique phosphomodifforms from the same protein may therefore provide information on the co-occurrence and potential cooperation of modifications, as well as their mutual exclusivity, on the same protein molecules (Fig. 4f).

HTP enables discovery of unannotated, functional phosphorylation sites in the proteome. An underlying hypothesis in this study was that the detection of significant modification-site-dependent changes in thermal stability would permit discovery of functional ‘hotspot’ sites that would be otherwise unannotated in the sea of undetected sites. We therefore investigated two previously reported yet uncharacterized phosphorylation sites associated with significant ΔT_m shifts for functional effects on protein activity.

The cytoskeletal protein vinculin exhibited an unmodified, bulk protein T_m that deviated significantly from its pS721 phosphomodiform (Fig. 5a). Published X-ray structures revealed that S721 lies at the N terminus of an α -helix in the D4 domain between the ‘head’ and ‘tail’ lobes of the protein (Fig. 5b), which regulates conformation switching³³ and subsequent vinculin clustering, binding to F-actin stress fibers and recruitment to focal adhesions³⁴. Given the proximity of S721 to contacts within the D4 domain, we hypothesized that the altered stability in response to phosphorylation may reflect altered intramolecular contacts or be a functional consequence thereof. We therefore interrogated wild-type, nonphosphorylatable (S721A) and phosphomimetic (S721D) vinculin constructs for the formation of characteristic focal adhesions, the hallmark phenotype for proper function of this protein³⁵.

Immunofluorescent visualization of FLAG-tagged, wild-type vinculin in HeLa cells showed high localization to distal membrane regions, which overlapped with F-actin and a marker of focal adhesions, paxillin (Fig. 5c–f). Nonphosphorylatable S721A vinculin exhibited a similar overall distribution, with the majority of this mutant colocalizing to focal adhesions of similar size and number per cell (Fig. 5c,d). The phosphomimetic S721D mutant vinculin displayed a highly significant, twofold reduction in vinculin/paxillin colocalization compared with cells expressing the S721A mutant, as well as a 58% reduction in the average size of the vinculin clusters (Fig. 5e,f). These data are consistent with a model where phosphorylation at S721 disrupts contacts in the closed form, and may stabilize an alternative, inactive conformation with diminished recruitment to focal adhesion complexes. Furthermore, we posit that the observed changes in thermal stability of the pS721 vinculin phosphomodiform may be capturing both a conformation change resulting from perturbed intramolecular contacts, as well as the stabilization of an alternative conformational state that is then capable

of engaging in new intermolecular interactions. These data provide a proof-of-concept example of the effective prioritization and discovery of uncharacterized, but phenotypically relevant, hotspot modification sites by HTP.

We next interrogated the pS210 phosphomodiform of the glycolytic enzyme glyceraldehyde-3-phosphate dehydrogenase (GAPDH), which was significantly destabilized relative to the unmodified, bulk GAPDH pool, as well as GAPDH protein that is unambiguously unphosphorylated at S210 (Fig. 6a). Other detected sites, such as pT154, were not associated with a significant ΔT_m shift (Supplementary Fig. 5a). Published structures show that S210 packs closely to L194 and by extension K195, which is involved in substrate binding (Fig. 6b). To explore the possibility that phosphorylation may affect GAPDH substrate binding and catalysis, and to extend HTP profiling to kinetic/signaling conditions, we performed HTP on cells under the limiting metabolic environment of acute glucose withdrawal, which depleted cellular glyceraldehyde-3-phosphate (GAP) levels fourfold (Supplementary Fig. 5b). Under these conditions the thermal shift between the bulk, unmodified GAPDH pool and the pS210 phosphomodiform disappeared (Fig. 6c). Specifically, the stability of the pS210 phosphomodiform was not affected by the presence of lower GAP levels, which contrasted with the significant destabilization of the bulk, unmodified GAPDH protein pool (Fig. 6d,e). These data suggested that GAP binding contributes to the stability of GAPDH protein that is not phosphorylated at S210, and the negative shift in stability associated with the pS210 phosphomodiform may be capturing the reduced substrate occupancy of these proteins in cells (Fig. 6f).

To specifically test GAP binding and metabolism we tested the enzyme kinetics of wild-type GAPDH relative to mutants that are incapable of phosphorylation (S210A) or that mimic phosphorylation (S210D). Indeed, the reaction kinetics and Michaelis constant (K_m) value for GAP was indistinguishable between the nonphosphorylatable S210A mutant and the wild-type enzyme (Fig. 6g,h), whereas the phosphomimetic S210D mutant remained active but exhibited decreased kinetics and a significantly increased K_m , consistent with altered ability to bind GAP (Fig. 6f). These effects were unique to S210, as the kinetics of nonphosphorylatable and phosphomimetic mutants for a nearby detected site, T182, did not affect conversion rates or K_m value for GAP (Supplementary Fig. 5c–e). These data confirmed that altered modiform–ligand interactions can be discovered and characterized by HTP profiling under basal and altered metabolic conditions.

Discussion

Here we established a proteomic method enabling the unbiased, global detection of protein stability changes in response to site-specific phosphorylation events on thousands of proteins. In contrast to traditional discovery-mode LC–MS/MS studies, the HTP method provides several novel insights into the functional effects of protein PTMs. First, it provides site-specific, quantitative relationships between the ‘unmodified, bulk’ population of a protein and its distinct phosphomodifforms in the endogenous context of live cells. We have demonstrated that this format promotes detection of both intrinsic alterations in protein structure, as well as context-specific intermolecular events, such as protein–protein and protein–metabolite interactions¹⁵. We posit that the ability to perform HTP profiling under steady-state and comparative kinetic conditions in response to small molecules or signaling events can be used to discover and characterize PTM-mediated interactions. We demonstrated this attribute of HTP through the identification of previously uncharacterized phosphorylation sites in well-characterized proteins, such as GAPDH, as well as less well-studied structural proteins, such as vinculin.

The information gained through HTP profiling of phosphomodifforms adds another functional layer to that measured by

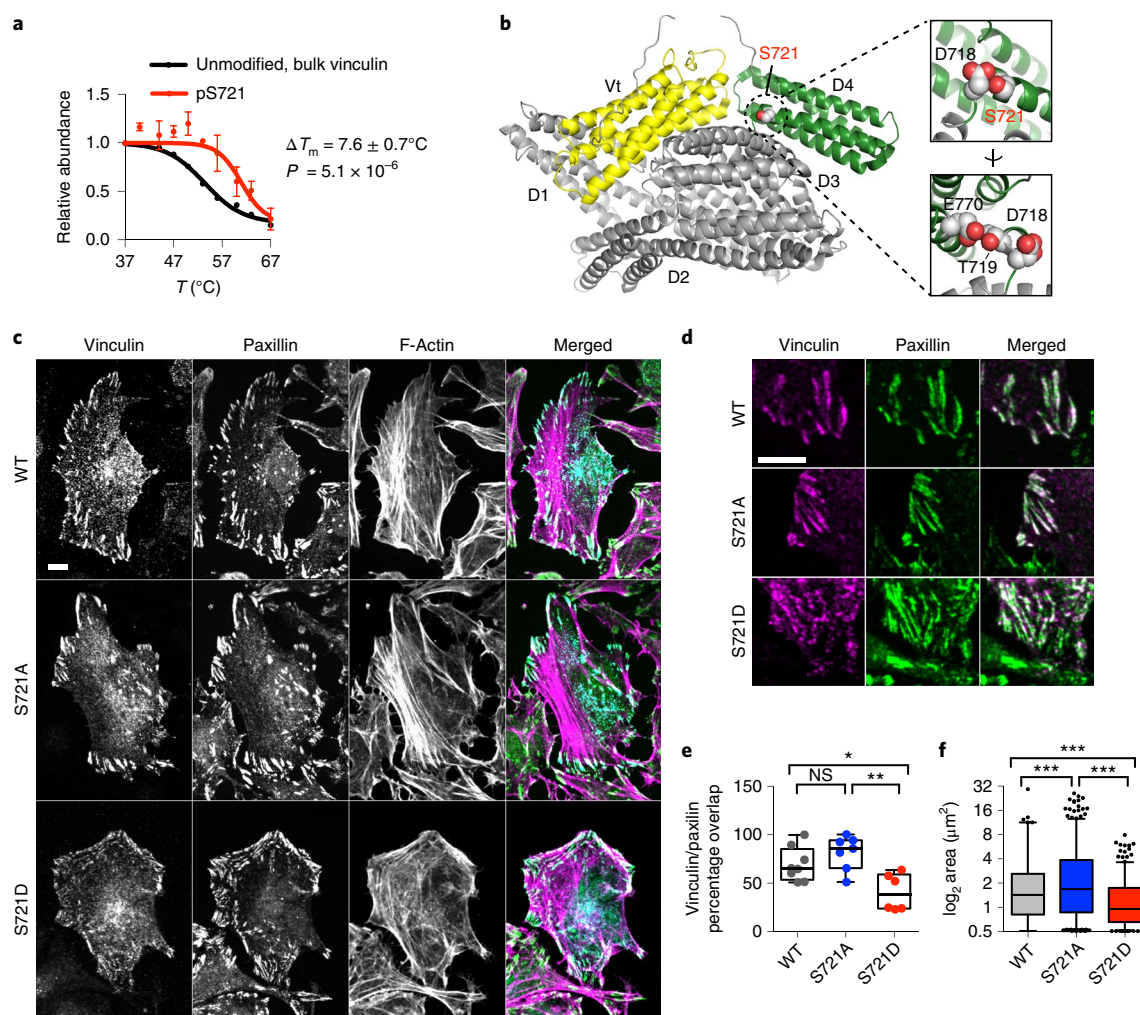


Fig. 5 | HTP discovery of an uncharacterized phosphorylation site in vinculin that regulates focal adhesion phenotypes. **a**, HTP curves for the unmodified, bulk and pS721 phosphomodiform of vinculin. **b**, X-ray structure of human vinculin with the uncharacterized phosphorylation site S721 shown as spheres packed in between the Vt (yellow) and D4 (green) domains. PDB 1TR2. Inset images show close contacts between S721, D718, T719 and E770, which cap a buried helix in the D4 domain. **c**, Confocal microscopy of wild-type, S721A and S721D FLAG-tagged vinculin constructs transiently expressed in HeLa cells. Merged, individual and colocalization channels are shown for vinculin (cyan), paxillin (green) and actin (purple). **d**, Representative focal adhesions at migrating fronts of the cell membrane are highlighted, and show significant phenotypic differences between the three vinculin constructs. **e**, Colocalization of vinculin and paxillin at paxillin-positive focal adhesions, where each point represents percentage colocalization in a quantified cell ($n=8$, 7 and 6 cells, respectively). **f**, Size of WT, S721A and S721D-vinculin focal adhesions in $n=8$, 7 and 6 cells, respectively. Each point represents a distinct focal adhesion. Scale bars, 10 μm . Data points shown in **a** represent the mean and s.e.m. from $n=6$ (bulk, unmodified) and $n=5$ (phospho) independent biological replicates. ΔT_m P value in **a** computed with two-sided t -test. Images shown in **c,d** are representative of three independent biological replicates. Box plots (median, 1–99%) are shown in **e,f**; $*P \leq 0.05$, $**P \leq 0.001$, $***P \leq 0.0001$, NS $P > 0.05$, one-way ANOVA.

quantifying the abundance of modification sites in the proteome, which report on relative ‘writing’ and ‘erasing’ of modifications across the proteome, but provide no information on the dynamic biophysical ‘reading’ of these modifications. HTP profiling alone, or in concert with datasets focused on mapping protein–protein¹⁹ and protein–metabolite^{15,17} interactions, will provide insights into the functional and interconnected roles of site-specific modification in the proteome.

It is important to consider the limitations of HTP-derived ΔT_m values in assuming functional impact on a protein of interest. First, this method specifically interrogates the inclusive pool of proteins that unambiguously contain a defining modification site, which we have described here as a ‘modiform’. Thus, this method cannot determine the modification status of other sites that do not fall within this peptide on the same protein molecule, a limitation that is intrinsic to massively parallel detection by LC–MS/MS. We do not

view this aspect of the approach as a limitation per se, because the primary goal of the approach is to correlate specific modification sites with putative changes to protein structure and function in cells, regardless of the inherent heterogeneity of the protein pool. As such, HTP may under-sample certain combinations of modifications, or miss them entirely, but it can unequivocally connect changes in apparent stability to the presence of site-specific, ‘hotspot’ modifications. Additionally, the response of individual phosphomodiforms to thermal challenge under a defined cellular condition may be used to provide information about the co-occurrence or mutual exclusivity of specific modification sites on the same molecules in the larger protein pool, as discussed here for TPI1, 4EBP1 and GAPDH. While beyond the scope of the current article, we hope that focused bioinformatic analyses of future datasets could shed light on this aspect of the HTP method. Finally, the method is intended to globally interrogate native, modified proteins in relevant biological contexts,

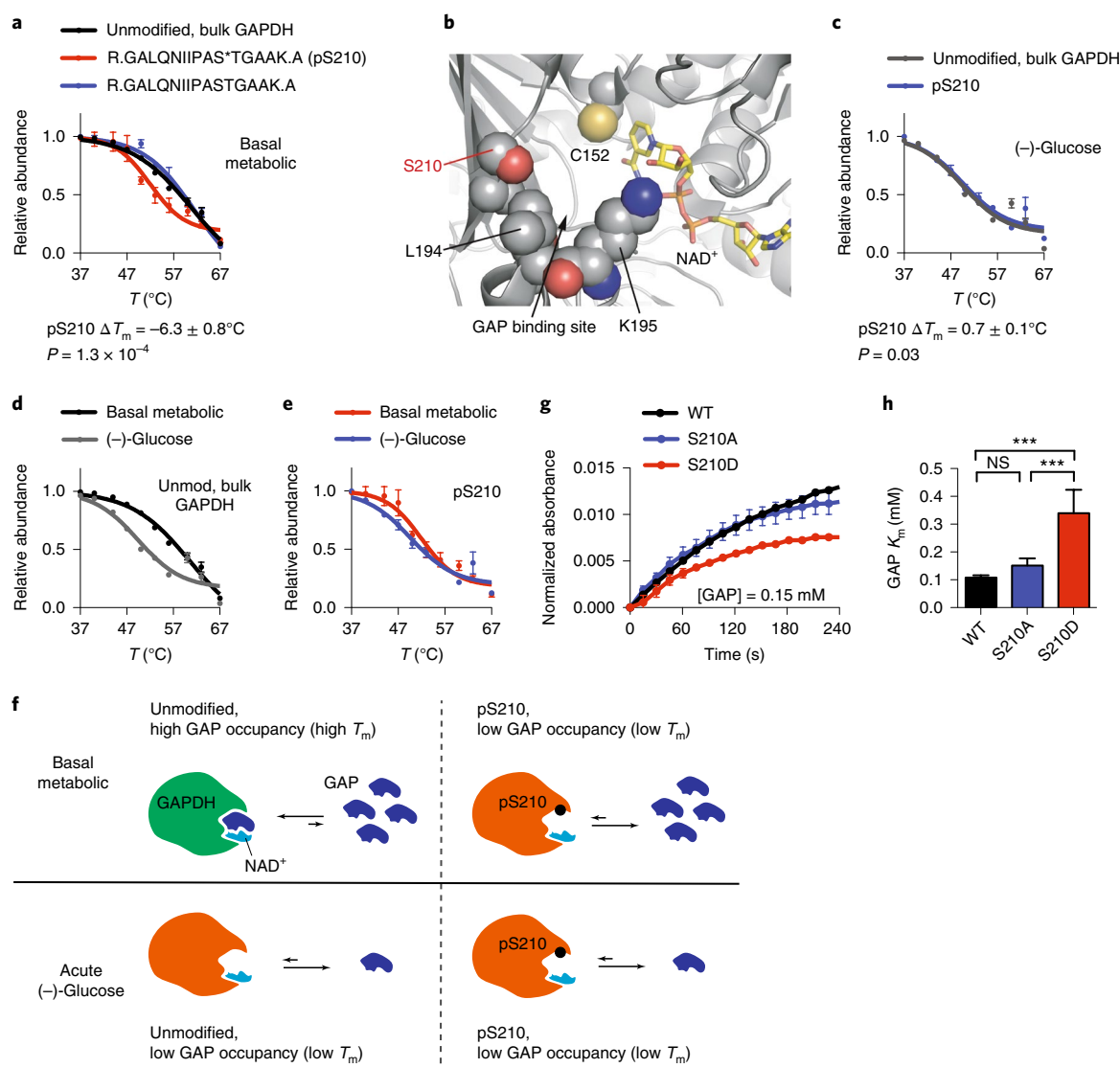


Fig. 6 | Discovery of a previously uncharacterized phosphorylation site affecting GAPDH catalysis. **a**, Representative HTP curves for the bulk, unmodified GAPDH and corresponding modifforms in HEK293T cells. **b**, X-ray structure of human GAPDH active site (gray) bound to NAD⁺ (tan). The site of phosphorylation, S210 and adjacent residues lining the GAP substrate-binding site are shown as spheres. PDB 1Z9Q. **c–e**, HTP curve comparisons for unmodified (**c,d**) and pS210 GAPDH (**c,e**) in cells after acute glucose restriction. **f**, Proposed model correlating high thermal stability of nonphosphorylated GAPDH bound to GAP in basal metabolic condition, and low thermal stabilities of pS210 in both basal metabolic and acute glucose withdrawal conditions. **g,h**, Representative in vitro kinetic measurement (**g**) and Michaelis-Menten kinetic analysis (**h**) of wild-type, S210A and S210D mutant GAPDH confirmed a significant increase in K_m toward GAP for the phosphomimetic enzyme ($***P \leq 0.0001$, two-sided *t*-test). Data points shown in **a,c–e**, represent the mean and s.e.m. from $n = 12, 3, 8, 3$ and 2 (in order of T_m curve appearance) replicate measurements detected in $n = 6$ (bulk, unmodified), $n = 5$ (phospho) and $n = 2$ (acute (-)-glucose, both bulk, unmodified and phospho) independent biological replicates. Data in **g,h** represent mean and s.e.m. from $n = 4$ technical replicates from $n = 2$ independent biological replicates.

to identify and prioritize sites for further study and to provide mechanistic hypotheses for functional validation. More than 90% of the modifications detected here have been previously observed in numerous datasets, but have no functional annotation, thus underscoring the low-throughput nature of current PTM annotation. We expect that the phosphorylation dataset presented here, as well as the extension of the HTP method to diverse organisms, cell types and PTMs will greatly expand our current understanding of the role of protein modifications in regulating protein structure, function and signal transduction.

Online content

Any methods, additional references, Nature Research reporting summaries, source data, statements of code and data availability and

associated accession codes are available at <https://doi.org/10.1038/s41592-019-0499-3>.

Received: 31 October 2018; Accepted: 21 June 2019;
Published online: 5 August 2019

References

- Agapakis, C. M., Boyle, P. M. & Silver, P. A. Natural strategies for the spatial optimization of metabolism in synthetic biology. *Nat. Chem. Biol.* **8**, 527–535 (2012).
- Yu, C. S., Chen, Y. C., Lu, C. H. & Hwang, J. K. Prediction of protein subcellular localization. *Proteins* **64**, 643–651 (2006).
- Gawron, D., Ndah, E., Gevaert, K. & Van Damme, P. Positional proteomics reveals differences in N-terminal proteoform stability. *Mol. Syst. Biol.* **12**, 858 (2016).

4. Walsh, C. *Posttranslational Modification of Proteins: Expanding Nature's Inventory* (Roberts and Company, 2006).
5. Hunter, T. Tyrosine phosphorylation: thirty years and counting. *Curr. Opin. Cell Biol.* **21**, 140–146 (2009).
6. White, F. M. & Wolf-Yadlin, A. Methods for the analysis of protein phosphorylation-mediated cellular signaling networks. *Annu. Rev. Anal. Chem. (Palo Alto Calif.)* **9**, 295–315 (2016).
7. Martin, L., Latypova, X. & Terro, F. Post-translational modifications of tau protein: implications for Alzheimer's disease. *Neurochem. Int.* **58**, 458–471 (2011).
8. Aebersold, R. & Mann, M. Mass-spectrometric exploration of proteome structure and function. *Nature* **537**, 347–355 (2016).
9. Huttlin, E. L. et al. A tissue-specific atlas of mouse protein phosphorylation and expression. *Cell* **143**, 1174–1189 (2010).
10. Olsen, J. V. & Mann, M. Status of large-scale analysis of post-translational modifications by mass spectrometry. *Mol. Cell. Proteom.* **12**, 3444–3452 (2013).
11. Walther, T. C. & Mann, M. Mass spectrometry-based proteomics in cell biology. *J. Cell Biol.* **190**, 491–500 (2010).
12. Humphrey, S. J., Azimifar, S. B. & Mann, M. High-throughput phosphoproteomics reveals in vivo insulin signaling dynamics. *Nat. Biotechnol.* **33**, 990–995 (2015).
13. Olsen, J. V. et al. Quantitative phosphoproteomics reveals widespread full phosphorylation site occupancy during mitosis. *Sci. Signal.* **3**, ra3 (2010).
14. Tsai, C. F. et al. Large-scale determination of absolute phosphorylation stoichiometries in human cells by motif-targeting quantitative proteomics. *Nat. Commun.* **6**, 6622 (2015).
15. Huber, K. V. et al. Proteome-wide drug and metabolite interaction mapping by thermal-stability profiling. *Nat. Methods* **12**, 1055–1057 (2015).
16. Martinez Molina, D. et al. Monitoring drug target engagement in cells and tissues using the cellular thermal shift assay. *Science* **341**, 84–87 (2013).
17. Piazza, I. et al. A map of protein-metabolite interactions reveals principles of chemical communication. *Cell* **172**, 358–372.e23 (2018).
18. Savitski, M. M. et al. Tracking cancer drugs in living cells by thermal profiling of the proteome. *Science* **346**, 1255784 (2014).
19. Tan, C. S. H. et al. Thermal proximity coaggregation for system-wide profiling of protein complex dynamics in cells. *Science* **359**, 1170–1177 (2018).
20. Smith, L. M. & Kelleher, N. L. Consortium for Top Down Proteomics Proteoform: a single term describing protein complexity. *Nat. Methods* **10**, 186–187 (2013).
21. Fermin, D., Walmsley, S. J., Gingras, A. C., Choi, H. & Nesvizhskii, A. I. LuciPHOR: algorithm for phosphorylation site localization with false localization rate estimation using modified target-decoy approach. *Mol. Cell. Proteom.* **12**, 3409–3419 (2013).
22. McGowan, C. H. & Russell, P. Human Wee1 kinase inhibits cell division by phosphorylating p34cdc2 exclusively on Tyr15. *EMBO J.* **12**, 75–85 (1993).
23. Watanabe, N., Broome, M. & Hunter, T. Regulation of the human WEE1Hu CDK tyrosine 15-kinase during the cell cycle. *EMBO J.* **14**, 1878–1891 (1995).
24. Blangy, A. et al. Phosphorylation by p34cdc2 regulates spindle association of human Eg5, a kinesin-related motor essential for bipolar spindle formation in vivo. *Cell* **83**, 1159–1169 (1995).
25. Azimi, A. et al. Targeting CDK2 overcomes melanoma resistance against BRAF and Hsp90 inhibitors. *Mol. Syst. Biol.* **14**, e7858 (2018).
26. Gnad, F. et al. PHOSIDA (phosphorylation site database): management, structural and evolutionary investigation, and prediction of phosphosites. *Genome Biol.* **8**, R250 (2007).
27. Jimenez, J. L., Hegemann, B., Hutchins, J. R., Peters, J. M. & Durbin, R. A systematic comparative and structural analysis of protein phosphorylation sites based on the mtcPTM database. *Genome Biol.* **8**, R90 (2007).
28. Kallberg, M. et al. Template-based protein structure modeling using the RaptorX web server. *Nat. Protoc.* **7**, 1511–1522 (2012).
29. Lee, T. Y. et al. dbPTM: an information repository of protein post-translational modification. *Nucleic Acids Res.* **34**, D622–D627 (2006).
30. Beretta, L., Gingras, A. C., Svitkin, Y. V., Hall, M. N. & Sonenberg, N. Rapamycin blocks the phosphorylation of 4E-BP1 and inhibits cap-dependent initiation of translation. *EMBO J.* **15**, 658–664 (1996).
31. Sekiyama, N. et al. Molecular mechanism of the dual activity of 4EGI-1: dissociating eIF4G from eIF4E but stabilizing the binding of unphosphorylated 4E-BP1. *Proc. Natl Acad. Sci. USA* **112**, E4036–E4045 (2015).
32. Gingras, A. C. et al. Regulation of 4E-BP1 phosphorylation: a novel two-step mechanism. *Genes Dev.* **13**, 1422–1437 (1999).
33. Garakani, K., Shams, H. & Mofrad, M. R. K. Mechanosensitive conformation of vinculin regulates its binding to MAPK1. *Biophys. J.* **112**, 1885–1893 (2017).
34. Humphries, J. D. et al. Vinculin controls focal adhesion formation by direct interactions with talin and actin. *J. Cell Biol.* **179**, 1043–1057 (2007).
35. Chorev, D. S. et al. Conformational states during vinculin unlocking differentially regulate focal adhesion properties. *Sci. Rep.* **8**, 2693 (2018).

Acknowledgements

We thank M. Rust for discussions surrounding the manuscript and G. Li for discussions regarding microscopy. We are grateful for financial support for this work from the following: Kwanjeong Educational Fellowship (to G.L.); NIH training grant no. GM007183 and National Academy of Sciences Ford Foundation Fellowship (to K.E.C.); NIGMS 1R01GM104032-01A1 (to M.L.G.); NCI R00CA175399 and NIGMS DP2GM128199-01 (to R.E.M.); The Dale F. Frey Award for Breakthrough Scientists from the Damon Runyon Cancer Research Foundation (to R.E.M.) and The University of Chicago.

Author contributions

J.X.H. designed and performed functional biochemical experiments, cell-based experiments, mass spectrometry experiments and analyzed data. G.L. designed, performed and analyzed mass spectrometry experiments. K.E.C. designed, performed and analyzed cell-based and microscopy experiments. J.W.C. performed mass spectrometry experiments and analyzed data. M.L.G. designed and supervised microscopy experiments and analyzed data. R.E.M. conceived of and supervised the study, designed, performed and analyzed experiments, and wrote the manuscript with input from all authors.

Competing interests

The authors declare no competing interests.

Additional information

Supplementary information is available for this paper at <https://doi.org/10.1038/s41592-019-0499-3>.

Reprints and permissions information is available at www.nature.com/reprints.

Correspondence and requests for materials should be addressed to R.E.M.

Peer review information: Allison Doerr was the primary editor on this article and managed its editorial process and peer review in collaboration with the rest of the editorial team.

Publisher's note: Springer Nature remains neutral with regard to jurisdictional claims in published maps and institutional affiliations.

© The Author(s), under exclusive licence to Springer Nature America, Inc. 2019

Methods

A Supplementary Protocol describing the HTP procedure is available and has also been deposited at ProtocolExchange³⁶.

Cell culture. HeLa and HEK293T cell lines were propagated in RPMI 1640 with 2 mM L-glutamine (HyClone) supplemented with 10% fetal bovine serum (Corning) and 1% penicillin–streptomycin (ThermoFisher Scientific). All cell lines were grown at 37 °C in a 5% CO₂ humidified incubator.

HTP proteomic sample preparation. HEK293 cells were grown to 90% confluency in 15 cm cell-culture-treated plates (Denville). Cells were scraped from plates, briefly washed and resuspended in PBS with EDTA-free protease inhibitor tablet (Roche) and phosphatase inhibitor cocktail 3 (Sigma-Aldrich) before being divided into ten equal aliquots. Each aliquot of live cells was exposed to a steady temperature between 37 °C to 67 °C for 3 min in parallel, incubated at 25 °C for another 3 min and lysed by rapid freeze–thawing. Insoluble proteins and cell debris were removed by centrifugation at 17,000g for 10 min. A small amount of supernatant from the 37 °C aliquot was set aside to use for protein quantification by Bradford's assay. The remaining fraction of whole-cell lysates was denatured in 8 M urea, followed by disulfide reduction with dithiothreitol (DTT) (10 mM, 30 min, 65 °C), alkylation (iodoacetamide, 15 mM, 30 min, room temperature, protected from light) and quenching (DTT, 5 mM, 10 min, room temperature). The proteome solution was diluted fourfold with ammonium bicarbonate solution (50 mM, pH 8.0), CaCl₂ added (1 mM) and digested with sequencing grade trypsin (~1:100 enzyme:protein ratio; Thermo Pierce) at 37 °C while rotating overnight. Peptide digestion reactions were stopped by acidification to pH 2–3 with 1% formic acid, and peptides were then desalted with Sep-Pak tC18 cartridges (50 mg, Waters), dried under vacuum, resuspended with LC–MS grade water (Sigma-Aldrich) and then lyophilized. A small fraction (5%) reserved for bulk unmodified proteome thermal profiling was split from each aliquot and lyophilized separately.

Phosphopeptide enrichment and TMT labeling. The major fraction of lyophilized peptides (95%) was redissolved in 28.5% lactic acid (Sigma), 57% acetonitrile (LC–MS grade, Sigma), 0.28% trifluoroacetic acid (Sigma) and applied to TiO₂ spin tips (catalog no. 88303, ThermoFisher) for phosphopeptide enrichment according to the manufacturer's protocol. Eluted phosphopeptides were acidified with formic acid (pH 2–3), desalted using ZipTip C18 tips (100 µl, Millipore) and lyophilized. The two sets of peptides (phospho-enriched and unenriched) were separately labeled with 10-plex isobaric tandem mass tags (catalog no. 90406, ThermoFisher) according to the manufacturer's protocol with slight modification. TMT reagents were reconstituted to 8 mg ml⁻¹ in anhydrous acetonitrile (Sigma) and added to lyophilized peptides dissolved in 100 µl of 200 mM HEPES buffer, pH 8.0 (~8:1 reagent:peptide ratio). The labeling reaction was carried out at room temperature for 1 h with gentle shaking, and quenched with 5 µl of 5% hydroxylamine (ThermoFisher). Labeled peptides were combined into a single pool per experiment, acidified with formic acid (pH 2–3), desalted using ZipTip C18 tips (100 µl, Millipore) and lyophilized. The final processed peptides were dissolved in LC–MS/MS buffer A (H₂O with 0.1% formic acid, LC–MS grade, Sigma-Aldrich) for LC–MS/MS analysis.

Proteomic LC–MS/MS and data analysis. LC–MS/MS experiments were performed with an Easy-nLC 1000 ultra-high pressure LC system (ThermoFisher) using a PepMap RSLC C18 column (75 µm x 50 cm; 3 µm, 100 Å, ThermoFisher) heated to 40 °C coupled to a Q Exactive HF orbitrap and Easy-Spray nanosource (ThermoFisher). TMT-labeled digested peptides in MS/MS buffer A were injected onto the column and separated using the following gradient of buffer B (0.1% formic acid acetonitrile) at 300 nl min⁻¹: 0–10% buffer B in 5 min, 10–40% buffer B in 240 min, 40–90% buffer B over 6 min and hold at 90% for 20 min. MS/MS spectra were collected from 0 to 250 min using a data-dependent, top-10 ion setting with the following details: full MS scans were acquired at a resolution of 120,000, scan range of 375–1500 *m/z*, maximum injection time (IT) of 60 ms, automatic gain control target of 1 × 10⁶ and data collection in profile mode. MS/MS scans were performed by higher energy collisional dissociation fragmentation with a resolution of 60,000, automatic gain control target of 1 × 10⁵, maximum IT of 60 ms, normalized collision energy of 30 and data type in centroid mode. The isolation window for precursor ions was set to 1.0 *m/z* with an underfill ratio of 0.5%. Peptides with charge state 1 and undefined were excluded and dynamic exclusion was set to 20 s. Furthermore, the S-lens RF level was set to 60 with a spray voltage value of 2.60 kV and ionization chamber temperature of 300 °C.

MS² files were generated and searched using the ProLuCID algorithm in the Integrated Proteomics Pipeline (IP2) software platform. Human proteome data were searched using a concatenated target/decoy UniProt database (UniProt_Human_reviewed_04–10–2017.fasta). Basic searches were performed with the following search parameters: higher energy collisional dissociation fragmentation method; monoisotopic precursor ions; high resolution mode (three isotopic peaks); precursor mass range 600–6,000 and initial fragment tolerance at 600 ppm; enzyme cleavage specificity at carboxy (C)-terminal lysine and arginine residues with three missed cleavage sites permitted; static modification of +57.02146 on cysteine (carboxyamidomethylation), +229.1629 on N-terminal and lysine for

TMT-10-plex tag; four total differential modification sites per peptide, including oxidized methionine (+15.9949) and phosphorylation (+79.9663) on serine, threonine and tyrosine (only for phospho-enriched samples); primary scoring type by XCorr and secondary by Z-score; minimum peptide length of six residues with a candidate peptide threshold of 500. A minimum of one peptide per protein and half-tryptic peptide specificity were required. Starting statistics were performed with a Δ mass cutoff of 10 ppm with modstat and trypstat settings. False discovery rates (FDR) of peptide (spectral false positive rate) were set to 1%. TMT quantification was performed using the isobaric 10-plex labeling algorithm, with a mass tolerance of 5.0 ppm or less in cases where co-eluting peptides interfere. Reporter ions 126.127726, 127.124761, 127.131081, 128.128116, 128.134436, 129.131417, 129.13779, 130.134825, 130.141145 and 131.13838 were used for relative quantification. In general, all quantified peptides have a mass error within 3 ppm.

Modification site localization analysis. Phosphorylation site localization analysis was performed using the LuciPHOR algorithm available on the Integrated Proteomics Pipeline. A global FDR score was calculated for every detected phosphopeptide from each MS run. Phosphosites, and therefore phosphomodiforms, were included in the dataset only if they satisfied a global FDR localization score of <0.01.

Melting curve analyses. All detected phosphopeptides that map to the same phosphorylation sites were grouped together and given a new identifier (Gene_pSite; Supplementary Fig. 4). For example, four different tryptic peptides mapping to the same GAPDH phosphorylation site, pS210, were all detected: R.DGRGALQNIIPAS(79.9963)TGAAKAVGK.V, R.DGRGALQNIIPAS(79.9963)TGAAK.A, R.GALQNIIPAS(79.9963)TGAAKAVGK.V and R.GALQNIIPAS(79.9963)TGAAK.A. These peptides were systematically relabeled with the new custom identifier 'GAPDH_pS210'. TMT reporter ion intensities of phosphopeptides with the same identifier were combined for each temperature fraction from the same MS run (Supplementary Fig. 4). Fold change values were calculated using the lowest temperature fraction as the reference. Similarly, for the bulk unmodified proteome, TMT reporter ion intensities of all unmodified peptides mapped to the same protein were combined, and fold change values relative to the lowest temperature condition were calculated. To generate unmodified protein and phosphosite-specific melt curves, relative fold changes as a function of temperature was fitted to the equation derived from the chemical denaturation theory using the R package developed by Savitski et al.¹⁸. Values for T_m were calculated at the point at which the sigmoidal curve crosses the 0.5 fold change level. Only T_m values calculated from melting curves with curve $R^2 > 0.8$ were used in subsequent analyses. Shifts in T_m values (for example, ΔT_m) induced by phosphorylation were determined by subtracting the T_m of the unmodified protein from the T_m of the phosphomodiform:

$$\Delta T_m = T_m(\text{Phosphomodiform}) - T_m(\text{Unmodified, bulk protein})$$

Values for ΔT_m could only be calculated for phosphosites belonging to proteins that were also detected in the unmodified proteome. Values for ΔT_m were not determined for phosphosites that were detected in fewer than two MS technical replicates. The T_m values of all unmodified proteins and phosphorylation sites, and their ΔT_m values and *P* values, are summarized in Supplementary Tables 1 and 2.

Error analyses. In our workflow, a composite protein-level T_m was calculated by averaging T_m values derived from all detected tryptic peptides of the same protein. To estimate the overall 'base error' of our peptide-level T_m measurements, that is, on average, how far a peptide T_m value deviates from its composite protein-level T_m , we took four representative datasets and calculated the median peptide ΔT_m standard deviation (Supplementary Fig. 2). Every detected tryptic peptide was curve-fitted individually, as well as their composite protein, to calculate T_m values. Each dataset is comprised of 10,000–16,000 peptides and >2,900 protein melt curves. We then subtracted the composite protein-level T_m from each peptide-level T_m to obtain peptide ΔT_m values and calculated the standard deviation of each set of peptide ΔT_m values. We plotted the distributions of the peptide ΔT_m s.d. of the four representative datasets, which resulted in a median peptide ΔT_m s.d. between 1.3 and 1.5 °C. The average value of 1.4 °C was used as the vertical cutoff (also known as the smallest high-confidence ΔT_m value) in the ΔT_m volcano plot (Fig. 2c).

In-situ measurement of polar metabolome by LC–MS/MS. For acute glucose withdrawal studies, confluent 15 cm plates of HEK293T cells were switched from RPMI media containing 10 mM glucose into glucose-free RPMI media and grown for 30 min. For control cells the media was replaced with fresh, glucose-containing media. Under both conditions, cells were scraped into ice-cold PBS and isolated by centrifugation at 1,400g and 4 °C. Cell pellets were resuspended in 300 µl of an 80:20 mixture of MeOH:H₂O. Internal deuterated standards, 10 nmol d₃-serine, were added to the extraction solution for quantification and sample normalization. LC–MS/MS analysis was then performed as described³⁷.

Gel electrophoresis and western blot. To determine the effect of the 3-min heat pulses on global phosphorylation level, we exposed cells to the thermal profiling heat pulses as detailed above, but directly homogenized whole proteome by

addition of 4X Laemmli buffer containing 50 mM DTT (Supplementary Fig. 3). Samples were prepared for SDS–PAGE by heating to 95 °C for 5 min, cooled to room temperature, resolved on 10% SDS–PAGE gel and transferred onto nitrocellulose membranes by standard western blotting methods. Membranes were blocked in 2% BSA in TBS containing 0.1% Tween-20 (TBST) and probed with primary and secondary antibodies. Antibodies used in this study include: anti-pS/T/Y (1:1,000, ab15556, AbCam). Secondary anti-mouse (Licor) was used at 1:10,000 dilution in 2% BSA-containing TBST and incubated for 1 h before washing and imaging on a Licor infrared scanner. Densitometry measurements were performed with ImageJ software.

Vinculin expression and focal adhesion confocal microscopy assays. Full-length Myc-DDK-tagged-human vinculin (NM_003373, Origene) was used to generate mutants with PCR primers in Supplementary Table 3 according to the QuikChange II Site-Directed Mutagenesis Kit manufacturer protocol (200523, Agilent). HeLa cells were grown to 70% confluency in 6-well plates before transfection of 500 ng plasmid with Lipofectamine 2000 (Invitrogen). After 4 h, cells were reseeded onto round glass cover slides. After 24 hr cells were washed once with PBS and fixed at 4 °C for 10 min in 4% paraformaldehyde-containing PBS. Fixed cells were then washed three times with PBS, and blocked with 2% BSA with 0.05% Triton in PBS for 30 mins in room temperature. Slides were stained with primary antibodies rabbit α -FLAG (1:500, Cell Signaling) and mouse α -paxillin (1:100, Millipore) overnight at 4 °C. Cells were washed three times with 0.05% Tween in TBST for 5 mins and then stained with secondary antibodies Alexafluor488-conjugated goat- α -rabbit (1:200; Sigma-Aldrich), Alexa568-conjugated goat α -mouse (1:200; Sigma-Aldrich), and Alexa647-conjugated phalloidin (1:25, Invitrogen) for 30 mins in 37 °C. Finally, slides were washed three times with TBST and quickly dipped in DI water before mounting in Slow Fade Gold Antifade (ThermoFisher).

Images were taken using Metamorph (Molecular Devices) acquisition software on Nikon Eclipse Ti-PFS inverted microscope with a Yokogawa CSU-X1 confocal scanhead with Spectral Applied Research Laser Merge Module (491 nm, 561 nm and 643 nm lasers). Images were obtained using an Andor Zyla sCMOS camera with a $\times 60$ Plan Apo TIRF 1.49 numerical aperture objective (Nikon). Image processing and quantification was done in ImageJ. A single focal plane was acquired in which the lamella was in focus, as indicated by basal actin stress fibers stained with phalloidin and paxillin. Paxillin and vinculin channels were background subtracted. The paxillin channel was thresholded and made into a binary mask to calculate the area of focal adhesions as indicated by paxillin. The binary mask was then overlaid onto the vinculin channel for segmentation and area calculation (threshold at $0.5 \mu\text{m}^2$) of vinculin incorporation into the focal adhesions. For line scans analysis, fluorescence intensity line profiles over vinculin and paxillin channels were merged (raw images that were background subtracted) and done in ImageJ.

GAPDH expression, purification and kinetic assays. Full-length, human GAPDH (NM_002046, Origene) was used to generate GAPDH mutants using the QuikChange II Site-Directed Mutagenesis Kit according to the manufacturer's protocol (catalog no. 200523, Agilent). Mutant GAPDH plasmids were verified by sequencing (CMV (forward) and XL39 (reverse)). Wild-type and GAPDH mutants were transiently expressed from a pCMV6 entry vector with a C-terminal Myc-DDK tag in confluent 10-cm plates of HEK293T cells by transfection of 2 μg plasmid with Lipofectamine 2000 (Invitrogen) according to the manufacturer's protocol. After 24 h, cells were collected by scraping, pelleted by centrifugation, washed twice with PBS and lysed in PBS containing EDTA-free complete protease

inhibitor (Roche), pH 8.0. After ultracentrifugation, lysates were added to Anti-Flag M2 affinity resin (Sigma-Aldrich) and rotated overnight at 4 °C. Resins were washed five times with PBS before eluting bound protein with $3 \times$ FLAG-peptide ($100 \mu\text{g ml}^{-1}$, 150 μl , twice, Sigma-Aldrich) in PBS for 1 h. Relative protein levels were assessed by SDS–PAGE and enzymes were used without further purification.

Michaelis–Menten kinetic assays to assess the catalytic activities of GAPDH proteins were performed on a Tecan Infinite M200 plate reader. GAPDH proteins were supplemented with constant NAD^+ (0.278 mM) and serial threefold dilutions of D/L-glyceraldehyde-3-phosphate (1.36–0.0056 mM) and NADH production (340 nm absorbance) was monitored. Enzyme velocity at different GAP concentrations was measured in the first 4 min and K_m were generated by applying a Michaelis–Menten curve fit to the plot of enzyme velocity as a function of GAP concentrations in Prism5 software.

Kinase substrate motif analysis. Motif analysis was performed by comparing peptide sequences containing the target phosphorylation site to commonly described kinase/phosphatase substrate consensus motifs listed in the Human Protein Reference Database (http://www.hprd.org/serine_motifs). Nine common kinase motifs were chosen for this analysis.

Secondary structure, solvent accessibility and protein disorder prediction. Secondary structure, solvent accessibility and protein disorder were predicted using RaptorX (<http://raptorx.uchicago.edu>)²⁸ Protein FASTA sequences were uploaded to the RaptorX Structure Prediction portal as described. To calculate the secondary structure percentage, the number of residues predicted to be α -helix, β -sheet or loop was divided by the total number of residues of all detected proteins. The secondary structure percentage of the phosphosites was calculated by dividing the number of sites predicted to be α -helix, β -sheet or loop over the total number of detected phosphosites. Secondary structure elements, solvent accessibility and degree of disorder of detected phosphosites were plotted against their ΔT_m values.

Phosphosite annotation analysis. The number of annotations with site-specific biochemical studies was extracted from the PhosphoSite database (<https://www.phosphosite.org>) and plotted against ΔT_m values.

Reporting Summary. Further information on research design is available in the Nature Research Reporting Summary linked to this article.

Data availability

Primary data for proteomic analyses are available for download at: <ftp://massive.ucsd.edu/MSV000083786>; <https://doi.org/10.25345/C5CS7H>. Raw data used in this work that are not included in supplementary tables or raw mass spectrometry files are available upon request, which includes primary and processed microscopy image files. A Nature Research Reporting Summary is available.

References

- Huang, J. X., Lee, G. & Moellering, R. E. Discovery and interrogation of functional protein modifications by Hotspot Thermal Profiling. *Protoc. Exch.* <https://doi.org/10.21203/rs.2.10602/v1> (2019).
- Chang, J. W., Lee, G., Coukos, J. S. & Moellering, R. E. Profiling reactive metabolites via chemical trapping and targeted mass spectrometry. *Anal. Chem.* **88**, 6658–6661 (2016).

Reporting Summary

Nature Research wishes to improve the reproducibility of the work that we publish. This form provides structure for consistency and transparency in reporting. For further information on Nature Research policies, see [Authors & Referees](#) and the [Editorial Policy Checklist](#).

Statistical parameters

When statistical analyses are reported, confirm that the following items are present in the relevant location (e.g. figure legend, table legend, main text, or Methods section).

n/a Confirmed

- The exact sample size (n) for each experimental group/condition, given as a discrete number and unit of measurement
- An indication of whether measurements were taken from distinct samples or whether the same sample was measured repeatedly
- The statistical test(s) used AND whether they are one- or two-sided
Only common tests should be described solely by name; describe more complex techniques in the Methods section.
- A description of all covariates tested
- A description of any assumptions or corrections, such as tests of normality and adjustment for multiple comparisons
- A full description of the statistics including central tendency (e.g. means) or other basic estimates (e.g. regression coefficient) AND variation (e.g. standard deviation) or associated estimates of uncertainty (e.g. confidence intervals)
- For null hypothesis testing, the test statistic (e.g. F , t , r) with confidence intervals, effect sizes, degrees of freedom and P value noted
Give P values as exact values whenever suitable.
- For Bayesian analysis, information on the choice of priors and Markov chain Monte Carlo settings
- For hierarchical and complex designs, identification of the appropriate level for tests and full reporting of outcomes
- Estimates of effect sizes (e.g. Cohen's d , Pearson's r), indicating how they were calculated
- Clearly defined error bars
State explicitly what error bars represent (e.g. SD, SE, CI)

Our web collection on [statistics for biologists](#) may be useful.

Software and code

Policy information about [availability of computer code](#)

Data collection

1. Thermo Xcalibur, Qual Browser (Version 4.0.27.19) - Quantitative Proteomics
2. MetaMorph® Microscopy Automation & Image Analysis Software (Version 7.8.8.0) – Fluorescence Microscopy
3. Odyssey Infrared Imaging Software (Version 3.0) – Western Blots Imaging
4. i-control™ software for Tecan Infinite M200 – Absorbance Measurement
5. Agilent MassHunter Workstation Software -- Data Acquisition and Analysis for 6400 Series Triple Quadrupole program version B.06.00

Data analysis

1. ImageJ (Fiji version 2.0.0) - Densitometry
2. Integrated Proteomics Pipeline (IP2) (Version 6.0.2), ProLuCID algorithm, LuciPHOR algorithm - Quantitative Proteomics
3. RStudio (Version 1.1.463) – Melting curve analysis
4. TPP: Analyze thermal proteome profiling (TPP) experiments (R package version 3.10.0) – Melting curve analysis
5. RaptorX: raptorx.uchicago.edu - Protein secondary structure prediction
6. Graphs presented were generated in GraphPad Prism 5.0, with analysis algorithms indicated in figure legends
7. All figures were drawn in Adobe Illustrator CC 2018
8. Agilent MassHunter Workstation Software -- Data Acquisition and Analysis for 6400 Series Triple Quadrupole program version B.06.00

For manuscripts utilizing custom algorithms or software that are central to the research but not yet described in published literature, software must be made available to editors/reviewers upon request. We strongly encourage code deposition in a community repository (e.g. GitHub). See the Nature Research [guidelines for submitting code & software](#) for further information.

Data

Policy information about [availability of data](#)

All manuscripts must include a [data availability statement](#). This statement should provide the following information, where applicable:

- Accession codes, unique identifiers, or web links for publicly available datasets
- A list of figures that have associated raw data
- A description of any restrictions on data availability

Primary data for proteomic analyses have been uploaded to MassIVE (dataset DOI: 10.25345/C5CS7H). Raw files can be downloaded from <ftp://massive.ucsd.edu/MSV000083786>. All other data and materials are available upon reasonable request.

Field-specific reporting

Please select the best fit for your research. If you are not sure, read the appropriate sections before making your selection.

- Life sciences Behavioural & social sciences Ecological, evolutionary & environmental sciences

For a reference copy of the document with all sections, see [nature.com/authors/policies/ReportingSummary-flat.pdf](https://www.nature.com/authors/policies/ReportingSummary-flat.pdf)

Life sciences study design

All studies must disclose on these points even when the disclosure is negative.

Sample size	Sample size for cellular experiments were determined according to the minimal number of independent biological replicates powered to significantly identify an effect. In vitro experiments were performed in replicate independent measurements as indicated in the text.
Data exclusions	No data was excluded.
Replication	All experiments were independently replicated, with biological and technical replicates listed in the legends of the corresponding figures. All attempts at replication were successful.
Randomization	Randomization was not relevant in this study because no live organisms were used in this study.
Blinding	Blinding was not relevant in this study.

Reporting for specific materials, systems and methods

Materials & experimental systems

n/a	Involved in the study
<input checked="" type="checkbox"/>	<input type="checkbox"/> Unique biological materials
<input type="checkbox"/>	<input checked="" type="checkbox"/> Antibodies
<input type="checkbox"/>	<input checked="" type="checkbox"/> Eukaryotic cell lines
<input checked="" type="checkbox"/>	<input type="checkbox"/> Palaeontology
<input checked="" type="checkbox"/>	<input type="checkbox"/> Animals and other organisms
<input checked="" type="checkbox"/>	<input type="checkbox"/> Human research participants

Methods

n/a	Involved in the study
<input checked="" type="checkbox"/>	<input type="checkbox"/> ChIP-seq
<input checked="" type="checkbox"/>	<input type="checkbox"/> Flow cytometry
<input checked="" type="checkbox"/>	<input type="checkbox"/> MRI-based neuroimaging

Antibodies

Antibodies used

List of commercial antibodies used:
 [Antigen, Company (Cat. No, Lot#), Source, Dilutions]
 1. α -pS/T/Y, AbCam (ab15556), Mouse, 1:1000
 2. α -FLAG-M2, Sigma Aldrich (F1804), Mouse, 1:1000
 3. α -FLAG, Cell Signaling (14795, Lot 4), Rabbit, 1:500
 4. α -Paxillin, Millipore (Lot 2798599), Mouse, 1:100
 5. IRDye[®] 800CW α -Rabbit, Licor (925-32213, C80116-07), Donkey, 1:10000
 6. IRDye[®] 800CW α -Mouse, Licor (925-32211, C50129-02), Donkey, 1:10000
 7. Alexafluor488-Conjugated α -Rabbit, Sigma Aldrich (A11034, Lot 1937195), Goat, 1:200
 8. Alexa568-Conjugated Goat- α -Mouse, Sigma Aldrich (A11004, Lot 1698376), Goat, 1:200

Validation

Commercial antibodies were validated by relevant citations, validation statements provided by the manufacturer, and data provided in the manuscript.

Eukaryotic cell lines

Policy information about [cell lines](#)

Cell line source(s)

1. HEK293T (ATCC, CRL-3216)
2. HeLa (ATCC, CCL-2)

Authentication

None of the cell lines were profiled for authentication.

Mycoplasma contamination

Cells lines used in this study tested negative for mycoplasma contamination.

Commonly misidentified lines
(See [ICLAC](#) register)

No commonly misidentified cell lines were used in this study.